# Constraining temperature at depth of the Kakkonda geothermal field, Japan, using Bayesian rock-physics modelling of resistivity: Implications to the deep hydrothermal system

# Constraining temperature at depth of the Kakkonda geothermal field, Japan, using Bayesian rock-physics modelling of resistivity: Implications to the deep hydrothermal system

Kazuya Ishitsuka [a,*], Yusuke Yamaya [b], Norihiro Watanabe [b], Yosuke Kobayashi [c], Toru Mogi [d], Hiroshi Asanuma [b], Tatsuya Kajiwara [e], Takeshi Sugimoto [e], Ryoichi Saito [e]

[a] *Kyoto University, Nishikyo-ku, Kyoto, Japan*
[b] *Renewable Energy Research Center, National Institute of Advanced Industrial Science and Technology, Koriyama, Fukushima, Japan*
[c] *Muroran Institute of Technology, Mizumoto, Muroran, Japan*
[d] *Tokyo Institute of Technology, Meguro-ku, Tokyo, Japan*
[e] *Geothermal Engineering Co., Ltd., Takizawa, Iwate, Japan*

ABSTRACT

Temperature-at-depth estimation is important for assessing supercritical geothermal resources. Bayesian rock-physics modelling of electrical resistivity is effective for estimating temperatures at depth. In this study, we improved a previously proposed Bayesian framework and demonstrated its effectiveness by estimating subsurface temperatures in the Kakkonda geothermal field, Japan. The proposed framework allows the estimation of either effective porosities or salinities in addition to temperatures; further, we were able to constrain the possible states of the crustal fluid at depth based on the estimates. The estimated 3D temperature structure was consistent with available deep temperature logs. Furthermore, the estimated results suggest the existence of a magmatic-hydrothermal system at depth in the field.

## 1. Introduction

Geothermal resources situated at a considerable depth and high temperature are often called supercritical or superhot geothermal resources, as they may contain crustal fluid in supercritical condition (Dobson et al., 2017; Reinsch et al., 2017). These resources are attractive because of the high enthalpy of fluids present in them, which can generate a high amount of electricity (Dobson et al., 2017; Reinsch et al., 2017). Supercritical geothermal resources have been confirmed in Iceland (Elders et al., 2014; Friðleifsson et al., 2017) and may exist in several other locations worldwide (Okamoto et al., 2019). Evaluating the high temperature distribution and its characteristics is important to assess the potential of supercritical geothermal resources. However, as the number of wells that can be obtained at depth in a possible geothermal system is limited, a suitable method to evaluate temperature at depth based on observations is required.

Temperatures at depth can be estimated based on micro seismic events (Tosha et al., 1998; Tanaka and Ishikawa, 2002; Zuza and Cao, 2020) as well as geochemical analysis of hydrothermal minerals (Browne et al., 1978; Tole et al., 1993) and their fluid inclusions (Baker and Goldstein, 1990; Beauchampset al., 2021). In addition, the calibration of hydrothermal simulations provides the spatial distribution of temperatures that match observations (e.g., temperature and geophysical logs, and geophysical data) (O'Sullivan et al., 2001; Jalilinarabady et al., 2011; Gunnarsson et al., 2011). However, the temperatures inferred from micro seismic events and geochemical analysis are limited to the depth interval (e.g., the lower limit of micro seismic events) and surface or borehole samples, respectively. Hydrothermal simulation requires detailed geological and geophysical data, such as the spatial distribution of physical parameters in the constitutive equations and boundary conditions. Moreover, the calibration of hydrothermal simulations based on observations is a very time-consuming task. Spatial interpolation of temperatures, such as that performed in the kriging approach (Sepúlveda et al., 2012), has been a versatile method for understanding the spatial distribution of temperatures. However, its effectiveness is limited to depth values where temperature logs are available.

Subsurface resistivity distribution is estimated in geothermal fields

---

using magnetotelluric (MT) surveys (Mogi and Nakama, 1993; Heise et al., 2008; Tseng et al., 2020; Ardid et al., 2021a). Because temperature influences the bulk resistivity of rocks (Olhoeft, 1981; Kummerow and Raab, 2015; Nono et al., 2020), resistivity distribution from MT surveys could elucidate the temperature distribution at different depths in geothermal fields. Machine-learning frameworks have been proposed to estimate temperatures from the resistivities acquired through the MT method for geothermal applications. For example, a neural network has been used to estimate temperatures at depth by training the relationship between temperatures, resistivities, and locations in available wells (Spichak et al., 2013; 2015; Ishitsuka et al., 2018; 2021).

The Bayesian framework have been applied as another machine-learning strategy to utilise resistivity for estimating the deep temperature around the IDDP-2 well in Reykjanes, Iceland (Hokstad and Tänavsuu-Milkeviciene, 2017). Bayesian frameworks have helped quantify and reduce uncertainty when modelling multi-datasets for estimating shallow features in geothermal fields (Ardid et al., 2021a; 2021b). Ishitsuka et al. (2021) proposed a Bayesian rock-physics modelling to estimate deep temperatures using resistivity obtained from the MT method, available temperature logs, and the geological boundary that controls the temperature pattern. The method was applied to a natural-state simulation model of the Kakkonda geothermal field in Japan (Ishitsuka et al., 2021). Bayesian frameworks has also been applied for deep temperature estimation in the upper mantle (Afonso et al., 2016; Qashqai et al., 2018). Most of these Bayesian frameworks consider a rock-physics model to link temperatures and geophysical observations, enable the incorporation of geological characteristics, and determine the range and probabilities of parameters. Therefore, compared to a neural network framework, which struggles to elucidate the underlying basis on which the estimates are derived, Bayesian framework is advantageous for the estimation of temperatures at depth because the underlying assumptions and geological scenario considered for the analysis are apparent. Despite the advantages of the Bayesian framework, analyses of the characteristics of the method through applications in geothermal fields are limited. Furthermore, it is not necessarily clear how we can incorporate prior assumptions and/or possible geological scenarios into the Bayesian framework, especially for deep geothermal systems.

In this study, we improved the Bayesian rock-physics modelling proposed by Ishitsuka et al. (2021) and applied it to the Kakkonda geothermal field in northern Japan (Fig. 1a) to constrain temperature, effective porosity and salinity at depth. In particular, we considered a spatial continuity of temperature and examined the case where pore-fluid salinity is treated as a variable, which had not been addressed by Ishitsuka et al. (2021). The Kakkonda geothermal field is one of the largest and most active liquid-dominated geothermal system in Japan (Kato et al., 1993; Doi et al., 1998; 2000). In the field, a Quaternary tonalite pluton named the Kakkonda granite is present below the Tertiary formations that comprise a productive reservoir (Fig. 1b). The WD-1a well penetrated the Kakkonda granite and showed a high temperature gradient of about 0.32 °C/m and a maximum temperature of > 500 °C measured at a depth of 3729 m (Ikeuchi et al., 1998) (Fig. 1c), indicating that the Kakkonda field potentially comprises supercritical geothermal resources.

## 2. Methodology

### 2.1. Inverse modelling to estimate physical parameters based on resistivity

The rock-physics model expresses the relationship between the observed resistivity, $\gamma$, and the physical parameters $\theta$ (e.g., effective porosity and temperature of a discretised block).

$$\gamma = f_{RPM}(\theta) + \varepsilon \tag{1}$$

where $f_{RPM}$ represents the rock-physics model and $\varepsilon$ is the random error that describes the accuracy of the observation and the rock-physics model. We used the modified Archie's equation by Glover et al. (2000) as the rock-physics model in equation 2:

$$\gamma = \gamma_r(1-\phi)^{-(\log(1-\phi^m)/\log(1-\phi))} + \gamma_f \phi^{-m} \tag{2}$$

where $\gamma_r$ and $\gamma_f$ are the resistivity of dry rock and pore fluid, respectively. $m$ represents an exponent indicating the rock pore connectivity. Glover's equation considers both rock matrix and pore-fluid resistivity and is widely applied to interpret measured resistivities in hydrothermal systems in volcanic areas (Aizawa et al., 2009). Water-saturated rock resistivity is controlled by pore-fluid resistivity (Archie, 1942), whereas rock matrix resistivity slightly influences the observed resistivity when the effective porosity is very low.

For the dry rock resistivity ($\gamma_r$), we used the experimental resistivity values of granite up to a temperature of 800 °C (Olhoeft, 1981) (Fig. 2a). The experimental model shows that the resistivity decreases exponentially with increasing temperature. The pore fluid was assumed to be NaCl–H$_2$O, which can mimic magmatic fluid (Weis et al., 2012; Scott et al., 2015; Afanasyev et al., 2018). The NaCl–H$_2$O resistivity ($\gamma_f$) used in this study is based on experimental data of Sinmyo and Keppler (2017), which depends on salinity ($c$), pressure ($p$) and temperature ($T$). The $\gamma_f$ resistivity model is based on experiments at temperatures between 100 to 800 °C, pressures between 0 to 1 GPa, and salinities between 0.01–1 M (0.056–5.6 wt%) (Sinmyo and Keppler, 2017). Using
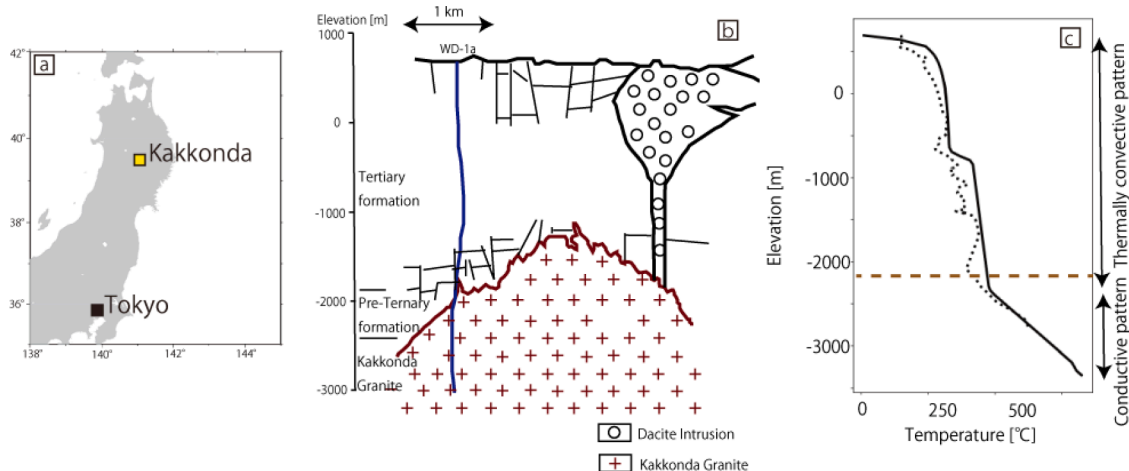


**Fig. 1.** (a) Location of the Kakkonda geothermal field. (b) Geological map of the Kakkonda geothermal field along a NW-SE cross section (based on Kato et al., 1996). (c) Reference natural-state temperature log (solid line) and observed temperature log (dotted line) along WD-1a well.
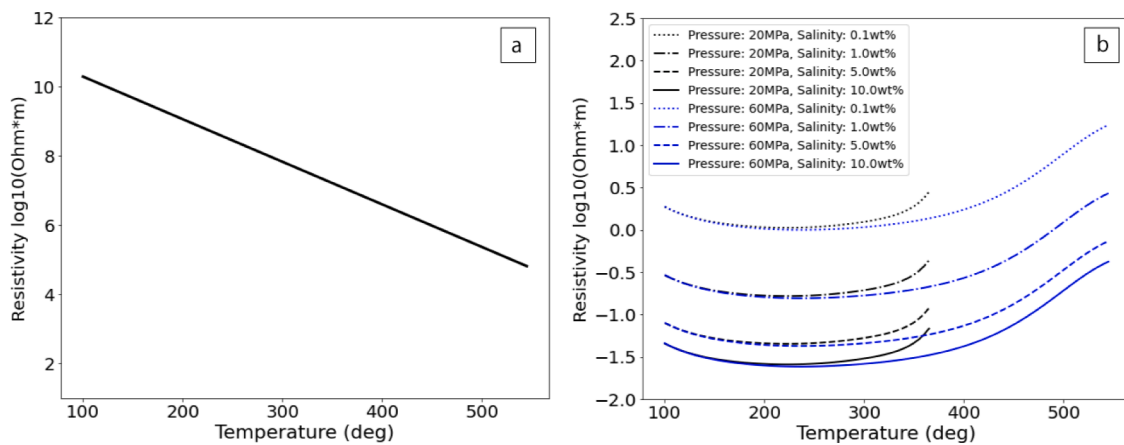
**Fig. 2.** Example of resistivity of (a) granite and (b) NaCl–H₂O as a function of temperature. In (b), resistivity was calculated with the method by Sinmyo and Keppler (2017) by assuming a salinity of 0.1, 1.0, 5.0, or 10.0 wt.% and pressure of 20 or 60 MPa.

the rock-physics model (Fig. 2b), assuming that the pore fluid is NaCl–H₂O, the physical parameters constitute five components: temperature, effective porosity, pressure, salinity, and the exponent $m$. More details on implementing the rock and NaCl–H₂O resistivities are presented in the Supplementary Material (Text S1).

Estimating temperatures at depth based on resistivity has the following characteristics: (i) Non-uniqueness, as resistivity can be interpreted based on multiple temperature states and physical quantities. (ii) Ill-posedness, since five physical parameters cannot be estimated from resistivity without assumptions. To address these issues, we propose the following processing steps (Fig. 3): Step 1 involves the estimation of 1D temperatures and either effective porosities or salinities at depth by using Bayesian rock-physics modelling. Pressure, the exponent $m$ of the rock-physics model, and either effective porosity or salinity are fixed in this 1D estimation (Fig. 3). By conducting the 1D estimation first, we mitigate the need for identifying numerous parameters for 3D estimation. To mitigate the non-uniqueness of temperature estimation from resistivity, the interpolated temperatures obtained from temperature logs were used to constrain the temperature above the upper boundary of the Kakkonda granite or at an elevation of −2000 m (with the upper boundary being deeper than an elevation of −2000 m), and temperatures below the boundary were estimated using Bayesian rock-physics modelling. This estimation is therefore an extrapolation of the temperature at depth based on the resistivity rock-physics model. In contrast, effective porosities or salinities were estimated at all depth intervals in this processing step. Although we used the interpolated temperatures as deterministic values in this study, the uncertainty in the interpolation could be considered and incorporated into a prior distribution of temperatures at the boundary, if available. Step 2 involves the estimation of a 3D temperature structure with spatial connectivity by fixing effective porosity and salinity based on the estimates obtained at step 1 (Fig. 3). In this step, the temperature estimates obtained in step 1 were the initial values used for sampling, and posterior probability distributions of the estimates were used as prior distributions of the 3D estimates.

## 2.2. Modelling using Bayes rule

In the Bayesian framework, the parameters and observations are represented by probability distribution functions (PDFs). The PDF of the estimated parameters, which represents the objective of the inversion, is denoted as the posterior PDF of the physical parameters according to available observations, $P(\theta|\gamma)$. The value corresponding to the highest PDF is termed the maximum *a posteriori* (MAP) estimate. We used the MAP estimate as a representative value because it arises most frequently. The posterior PDF in the Bayesian framework is defined by

the likelihood, $P(\gamma|\theta)$, and prior PDF, $P(\theta)$.

$$P(\theta|\gamma) \propto P(\gamma|\theta)P(\theta) \tag{3}$$

$P(\gamma|\theta)$ represents the fit between the model outputs $f_{RPM}(\theta)$ and observations $\gamma$, given the estimates of the physical parameters $\theta$. $P(\gamma|\theta)$ includes the effects of both observation errors and forward model uncertainties. $P(\theta)$ expresses uncertainty of the estimated parameters before any observations are made. Hence, $P(\theta)$ is controlled by expert knowledge of the estimated parameters. In this study, we used the likelihood function such that the discrepancy between observed resistivity and estimated resistivity follows a Gaussian distribution with a mean value of zero and the standard deviation of $\sigma_r$.

As $P(\theta|\gamma)$ is rarely solved analytically, it was assessed by sampling using a MCMC algorithm. An MCMC algorithm allows the sampling of an unknown probability distribution with known PDFs by an ensemble of chains using a stochastic process (Gelman et al., 2013). We used the No-U-Turn (NUTS) sampler with dual averaging (Hoffman and Gelman, 2014). This sampling method extends the Hamiltonian Monte Carlo (HMC) algorithm (Neal, 2011), which samples a chain based on a fictitious Hamiltonian dynamic. The HMC algorithm is superior to the existing MCMC algorithms such as Metropolis (Metropolis et al., 1953) and Gibb's sampling (Geman and Geman, 1984) with regard to its efficiency for suppressing random-walk behaviour; however, costly tuning runs are required to determine the optimal value of hyper parameters. The NUTS sampler with dual averaging allowed us to determine the optimal values automatically. For checking convergence, we used the $\hat{R}$ criterion (Gelman and Rubin, 1992) (Text S1). We used the Stan statistical package (version 2.19.2) (Carpenter et al., 2017) to implement the proposed Bayesian framework.

### 2.2.1. Depth models for 1D estimation of temperature, effective porosity, and salinity (step 1)

To constrain the search ranges of the two parameters (temperature and either effective porosity or salinity), we introduced the vertical correlations of each parameter as depth models. Regarding the temperature depth profile, deep locations where there are supercritical geothermal resources may exhibit thermally conductive properties because of low permeability. Actually, WD-1a reference temperatures below an elevation of −2350 m revealed thermally conductive properties (Fig. 1c). We thus modelled deep temperature by estimating a constant temperature gradient in the vertical direction. As an alternative option, vertical heat transfer by advection may be applied as a deep temperature model (Bredehoeft and Papadopulus, 1965) in the area where advective temperature profiles are expected.

For depth models of effective porosity and salinity, we parametrised the value using a state-space model of depth (Commandeur and
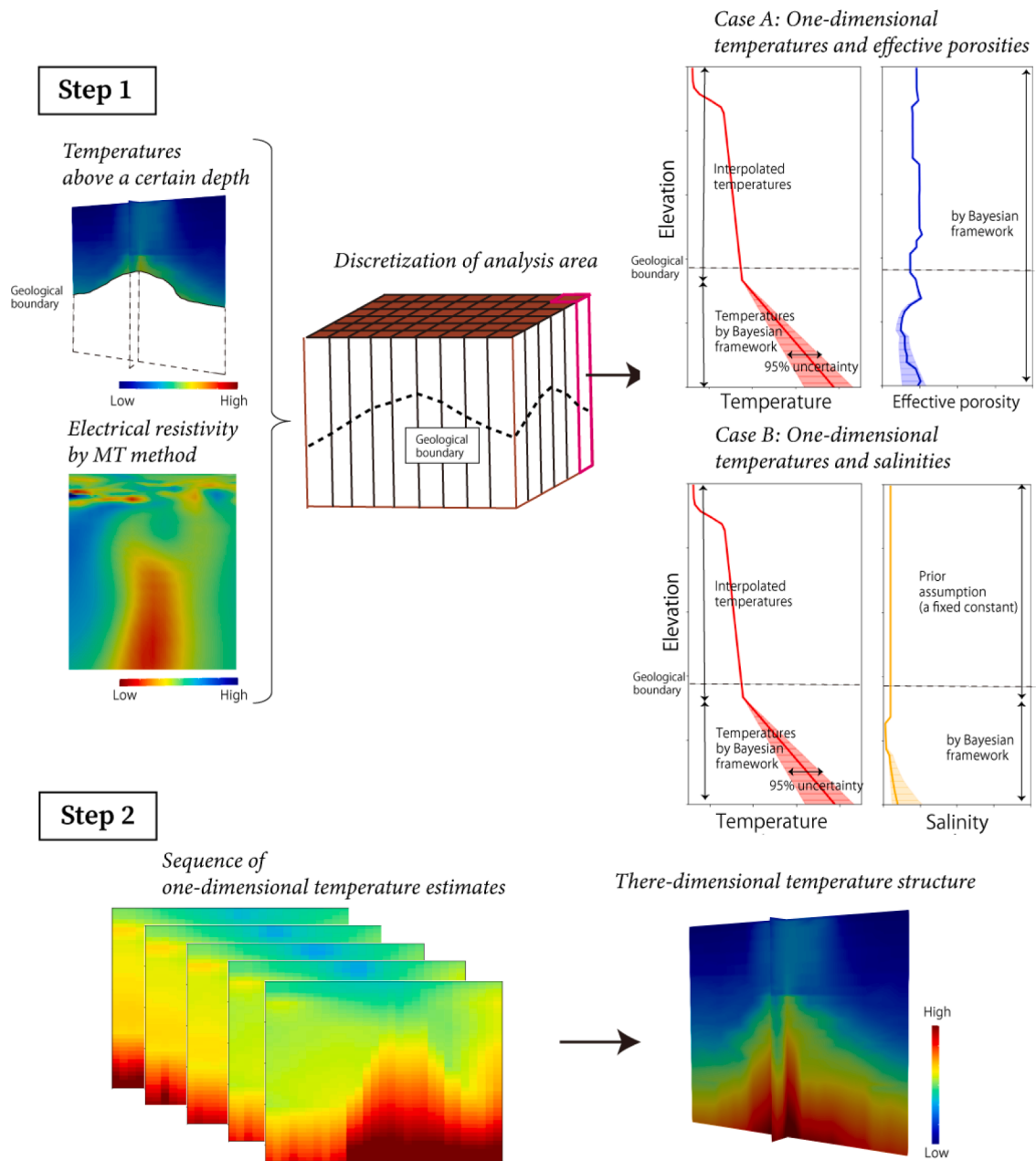
**Fig. 3.** Description of the processing steps: Step 1 conducts 1D (vertical) estimation of temperatures and either effective porosities or salinities using the proposed Bayesian framework. Temperatures are estimated only at depth below the geological boundary, using the interpolated temperature derived from temperature logs as the boundary condition for shallow areas. Effective porosities or salinities are estimated at all depth ranges. Step 2 estimates the 3D temperature structure with spatial continuity from the series of 1D temperature estimates obtained in step 1.

Koopman, 2007). The state-space model in this study used the Cauchy distribution for the state equation and the Gaussian distribution for the observation equation (Kitagawa, 1987, 1996) (Text S1). The Cauchy distribution is a heavy-tailed distribution wherein outliers occur more frequently compared to the Gaussian distribution. Therefore, the state-space model has been used to express abrupt changes in the regular trend (Kitagawa, 1996; Kitagawa and Matsumoto, 1996), and can thus be used to express a complex effective porosity or salinity pattern with different depths. We then compared two cases of model combinations. Case A was used as *a priori* (fixed) value for salinity based on geological assumptions, and effective porosity was estimated using the state-space model. Case B was used to fix effective porosity in the Kakkonda granite and estimate salinity using the state-space model.

The underlying idea of cases A and B is based on the phase diagram of

the NaCl–H$_2$O system. As the geologic environment above a magma chamber is considered to exhibit a high pressure and temperature, the exsolving magmatic fluid is assumed to be a single-phase fluid (Heinrich, 2007). As this magma-derived fluid ascends toward the surface, the pressure and temperature decrease gradually. Case A corresponds to the assumption that the magmatic fluid ascends without phase separation and salinity could be fixed as a constant through different depths. Case B may be a simple approximation of a result of the phenomena that the phase separates into a low-salinity/low-density vapour and a high-salinity/high-density liquid. Considering the phase diagram of the NaCl–H$_2$O system (Driesner and Heinrich, 2007; Driesner, 2007), the phase separation takes place when the pressure and temperature condition intersect the vapour + liquid coexistence surface, which is the boundary between a single-phase fluid and vapour + liquid coexistence

region. This phase separation causes the spatial variation of salinity in a magmatic-hydrothermal environment (Weis et al., 2012; Weis 2015; Scott et al., 2015, 2017; Afanasyev et al., 2018). Therefore, in case B, salinity should be a variable with a certain freedom, while effective porosity is fixed to make the inverse problem tractable. The parameters of the two cases are listed in Table S1. We note that our estimation did not solve the phase separation process and the two cases do not necessarily correspond to the temperature-pressure-salinity state of the phase diagram. In addition, to avoid the confusion about the term supercritical geothermal resources, we note that the deep geothermal resources can contain a single-phase supercritical and/or multiphase fluids, though the supercritical fluid is defined as a single-phase fluid in supercritical condition (Liebscher and Heinrich, 2007).

### 2.2.2. Temperature model for 3D estimation (step 2)

The spatial continuity of temperature can be expressed by the requirement of temperatures of neighbouring pixels being similar. In Bayesian rock-physics modelling, this requirement can be expressed by assuming that the difference in temperatures of neighbouring grid cells follows a Gaussian distribution with a constant variance and zero mean, which is termed the Gaussian conditional auto regressive (Gaussian CAR) model (Banerjee et al., 2015) (Text S1). In the 3D estimation, we set $\sigma_r$ prior to the Bayesian modelling. The $\sigma_r$ value can be tuned to show the spatial continuity of temperature. If $\sigma_r$ is low, the estimated temperature will be almost equal to the 1D estimation, and there will be spatial discontinuities. In contrast, if a high $\sigma_r$ value is used, spatially continuous temperatures can be estimated. By setting $\sigma_r$ as *a priori* information, a spatially continuous temperature can be estimated. However, $\sigma_r$ needs to be determined by trial and error. The examination of $\sigma_r$ by application to real data is described in Text S3. The processing step parameters are listed in Table S2.

## 3. Implementation of the model in the Kakkonda geothermal field

### 3.1. Kakkonda geothermal field

The Kakkonda geothermal field is located in northern Honshu, Japan (Fig. 1a). The Tertiary formations comprise andesite tuffs, sandstone, and slate (Fig. 1b). The productive reservoir lies in the Tertiary formations. A Quaternary tonalite pluton named the Kakkonda granite is below the Tertiary formations (Fig. 1b). The New Energy and Industrial Technology Development Organization (NEDO) drilled the WD-1a well to a depth of 3729 m (approximately −3020 m a.s.l) (Ikeuchi et al., 1998) (Fig. 1b). The well encountered the Kakkonda granite at −2150 m a.s.l. The temperature at the well bottom was estimated to be 500–510 °C using temperature melting tablets (Ikeuchi et al., 1998) (Fig. 1c). In the temperature profile of the WD-1a well, the temperature shows a convective pattern in the Tertiary formations, whereas the temperature pattern becomes conductive in the Kakkonda granite (Ikeuchi et al., 1998) (Fig. 1c). Kasai et al. (1998) found fluid inclusions with high-salinity in the WD-1a well, whereas the shallower part of the geothermal field is dominated by meteoric water. The high salinity at depth indicates that brine was trapped in pores and grain boundaries of minerals in the granite that originated from the solidification of magma (Kasai et al., 1998). Therefore, magmatic fluids may exist inside the Kakkonda granite.

### 3.2. Input and validation data preparation

Resistivity data were estimated using three-dimensional inversion analysis of MT data, which were obtained using previous geothermal surveys (NEDO, 1990, 1999; Uchida et al., 2000) and a recent supercritical geothermal resource project (Yamaya et al., 2021). Full impedance tensor values of 15 periods with durations between 0.0667 and 909 s were obtained at 74 stations (Fig. S2) that covered an area of 7 km

(NS) × 13 km (EW) centred around the Kakkonda power plant; these values were inverted using the magnetotelluric inversion program WSINV3DMT (Siripunvaraporn and Egbert, 2009). The estimated resistivity structure of the best-fit model was characterised using a conductive anomaly (<10 Ωm) corresponding to the upper central part of the Kakkonda granite (Fig. 4).

For the temperatures above the Kakkonda granite, we used the interpolated temperatures derived using the method in NEDO (2019) and Akatsuka et al., (under review) (Text S2). Temperature logs along the WD-1a well were used to evaluate the accuracy of the proposed methodology; as these were partly influenced by geothermal production, we corrected them based on fluid inclusions obtained from well cuttings/cores and surrounding natural-state temperature logs; subsequently, the corrected temperature log was used as the reference for the well (Fig. 1c). For validation, we also used the temperature log along Well-21, which is located approximately 1100 m southeast of WD-1a (Ikeuchi et al., 1998). Well-21 also penetrated the Kakkonda granite, where a conductive temperature pattern was also observed (Ikeuchi et al., 1998). As the temperature log along Well-21 was also affected by geothermal exploitation, we corrected it based on fluid inclusions and surrounding natural-state temperature logs.

As described in Section 3.1, the temperature within the Kakkonda granite shows a conductive temperature gradient, whereas the formations above and at the periphery of the Kakkonda granite show convective temperature profiles. The depth of the upper boundary of the Kakkonda granite along the wells was determined from the existence of Kakkonda granite and thermal metamorphic minerals identified in the drill cuttings. We used a kriging interpolation to calculate the spatial distribution of the upper boundary depth of the Kakkonda granite. The shallowest depth of the geological boundary is an elevation of approximately −500 m around the centre of the analysed area, and it deepens towards the periphery.

The lower and upper depth limits of the analysed area were selected to be −0.5 km and −2.7 km, respectively (Fig. 4). As the pore-fluid resistivity model was constructed up to 600 °C for the highest salinity, we set the lower depth limit to where the interpolated temperature was about 600 °C. For the upper depth limit, the depth was chosen to be deeper than the low resistivity zone due to the influence of clay minerals. Horizontally, the selected area is 4.35 km long in the EW direction and 4.05 km long in the NS direction, based on the geological boundary of the Kakkonda granite (Fig. 4). Resistivities and interpolated temperatures were discretised with a horizontal spacing of 150 m and a depth spacing of 50 m. Therefore, the number of grid cells in the EW and NS directions are 29 and 27, respectively, and 44 in the vertical direction.

### 3.3. Prior distributions and assumptions

A prior PDF was chosen as some externally defined quantity, based on a plausible geological scenario and/or a geophysical limitation. Effective porosities should be greater than 0 and may be less than 0.3 in the target depth interval. Therefore, we assigned a uniform distribution from 0 to 0.3. For the temperature gradient, we used a normal distribution with a mean of 0.35 °C/m and a standard deviation of 0.035. When salinity was regarded as a variable, we set the value to be positive. For the parameters that cannot be constrained from geological and geophysical viewpoints (e.g., variance), we used Student's half-t distribution as a prior PDF of the non-geophysical parameters as recommended in Gelman (2006).

The compilation of published fluid inclusion data suggests that the salinity of the pristine magmatic fluid is 2–10 wt% (Heinrich, 2005). In case A, we fixed the salinity profile, with the maximum value of 6 wt% as an average of the possible range of the pristine magmatic fluid (Fig. S3). On the other hand, in case B, effective porosity was fixed at 0.035, which is an average of the measured porosity of the Kakkonda granite (0.022–0.043) (Fujimoto et al., 2000). We used 1.5 for the exponent *m* of the rock-physics model (Eq. (2)) and compared the estimated result with
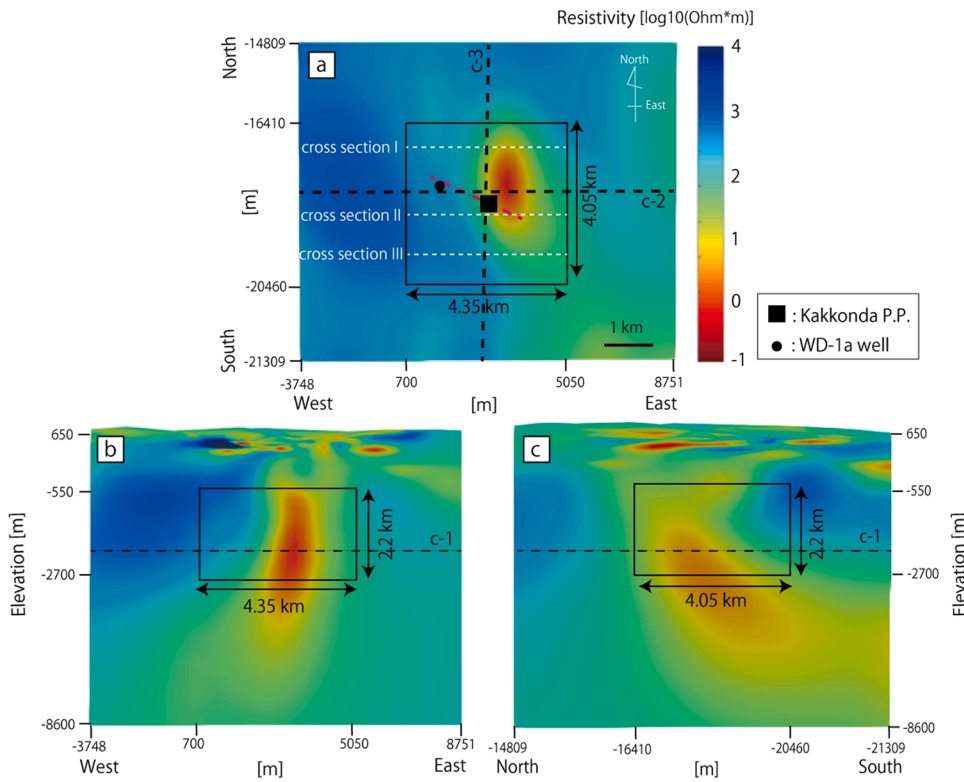
**Fig. 4.** Resistivity obtained using the MT method along the elevation of −2 km (a), EW cross section (b), and NS cross section (c). The location of the cross section (a) is plotted using black dashed lines in (b) and (c), whereas the locations of (b) and (c) are plotted using black dashed lines in (a). The black rectangle in (a) indicates the area analysed, and the white dashed lines in (a) indicate the locations of the cross sections provided in Fig. 6. The black square and circle in (a) indicate the locations of the Kakkonda power plant and WD-1a well, respectively. The location of the section in Fig. 1b is plotted using a pink dashed line in (a). The white dashed lines in (a) indicate the section shown in Fig. 6. The coordinates in the EW and NS directions are based on the Japan Geodetic Datum 2011 No.10 (reference coordinate: longitude = 140.83333 and latitude = 40.00000).

those obtained with $m = 2$. We assumed a lithostatic pressure with a rock density of 2600 kg/m$^3$. Considering that the observed temperatures show a change in the thermal conduction pattern at a depth slightly below the top of the granite (e.g., Fig. 1c), we set the boundary between interpolated temperatures and Bayesian estimation as 200 m below the top of the Kakkonda granite.

## 4. Results

### 4.1. Evaluation of 1D estimation using well data from WD-1a

We first evaluated our method of 1D estimation (step 1) using the WD-1a reference temperature log (solid line in Fig. 1c). As the result of the estimation, the maximum $\widehat{R}$ values in cases A and B were 1.07 and 1.13, respectively, which suggests that the MCMC samplings converged sufficiently. The MAP estimates and the credible interval at 95% along the well are shown in Fig. 5. The percentage errors of the estimated temperatures in the Kakkonda granite were 0.8% and 3.5%, respectively (Fig. 5). Because of the good agreement, we concluded that both cases enable the estimation of temperature-at-depth distribution with good accuracy. In contrast, estimated effective porosities and salinities were different between the cases. In case A, estimated effective porosities at different depths were <~0.02; this value was smaller than the fixed effective porosity of 0.035 in case B (Fig. 5). The estimated salinity in case B was <~3 wt%, whereas the fixed maximum salinity of 6.0 wt% was used in case A (Fig. 5). Regarding the exponent $m$, estimated temperatures when $m = 1.5$ were similar to those when $m = 2.0$, whereas the estimated porosities when $m = 1.5$ in case A were lower than those when $m = 2.0$ (Fig. S4). As the measured porosity of WD-1a rock core samples below an elevation of −2300 m was 0.022–0.035 (Fujimoto et al., 2000), $m = 1.5$ may be a more appropriate assumption compared to $m = 2.0$.

### 4.2. Estimation of temperature, effective porosity, and salinity distribution in the Kakkonda field

To confirm the convergence of the MCMC computation, we checked whether $\widehat{R}$ values of each 1D estimation were lower than the threshold ($\widehat{R} < 1.4$). Because the $\widehat{R}$ values in 95.9% of the locations (751 horizontal grid cells out of 783 (27 × 29)) in case A and 99.0% of the locations (775 horizontal grid cells out of 783 (27 × 29)) in case B were lower than 1.4 (Fig. S5), we considered that the MCMC calculations sufficiently converged and the estimates were statistically reliable. Furthermore, in cases A and B, the differences between MT resistivities and resistivities calculated by our analysis were small (< ± 0.05 $\Omega m$) (Fig. 6), indicating the parameters were properly estimated. The computational cost of the temperature estimation was approximately 30 min per 1D estimation when a personal computer with four AMD EPYC 7502P CPUs was used. Therefore, it took 392 h to conduct the calculation for all grid cells (i.e., 27 × 29 horizontal grid cells in total).

The cross sections of temperature-effective porosities (case A) and temperature-salinity (case B) were mapped and presented in Fig. 6. The cross sections enable an understanding of the general trend of the spatial temperature distribution; for example, in the central and eastern parts of the study area, the high temperature (>400 °C) region was estimated to exist at shallower depths (Fig. 6). The cross sections of estimated effective porosities in case A show that the background of effective porosities in the analysed area was low (<0.03), whereas relatively high effective porosities (>0.1) were estimated in accordance with low resistivities (<10 $\Omega m$) (Fig. 6a). In contrast, the cross sections in case B show that the low resistivity region corresponds to high salinity (>15%) around the bottom of the analysed area (Fig. 6b).

The estimated 3D temperature structure derived from the Gaussian CAR model is shown in Fig. 7. After testing the $\sigma_r$ values 0.01, 0.05, and 0.1, we selected $\sigma_r = 0.05$ as an optimal value (Fig. S6 and text S3). The computational cost of the 3D temperature estimation was approximately 26 h. Compared with the WD-1a reference temperature, the percentage errors below an elevation of −2350 m (below the upper boundary of the
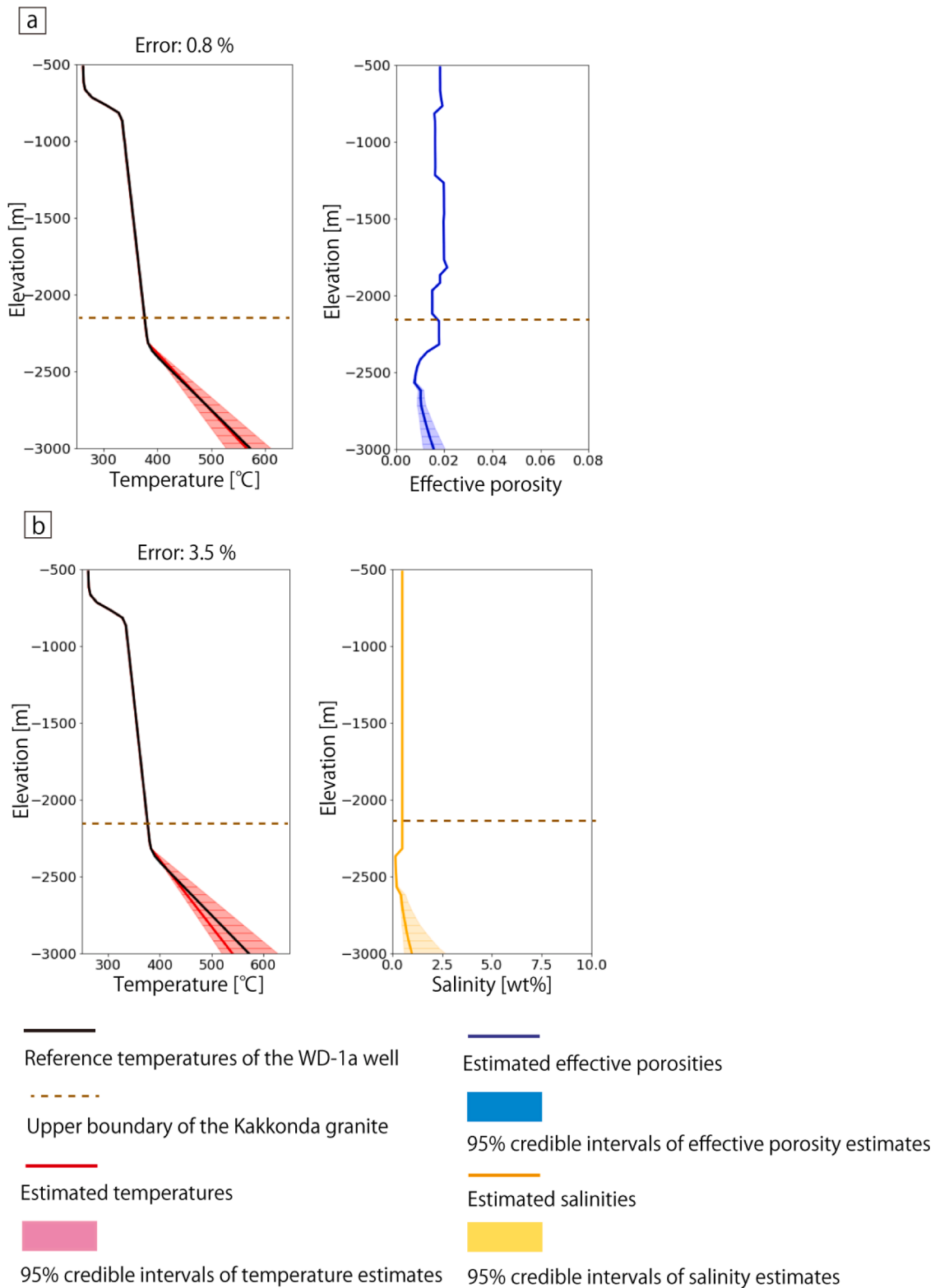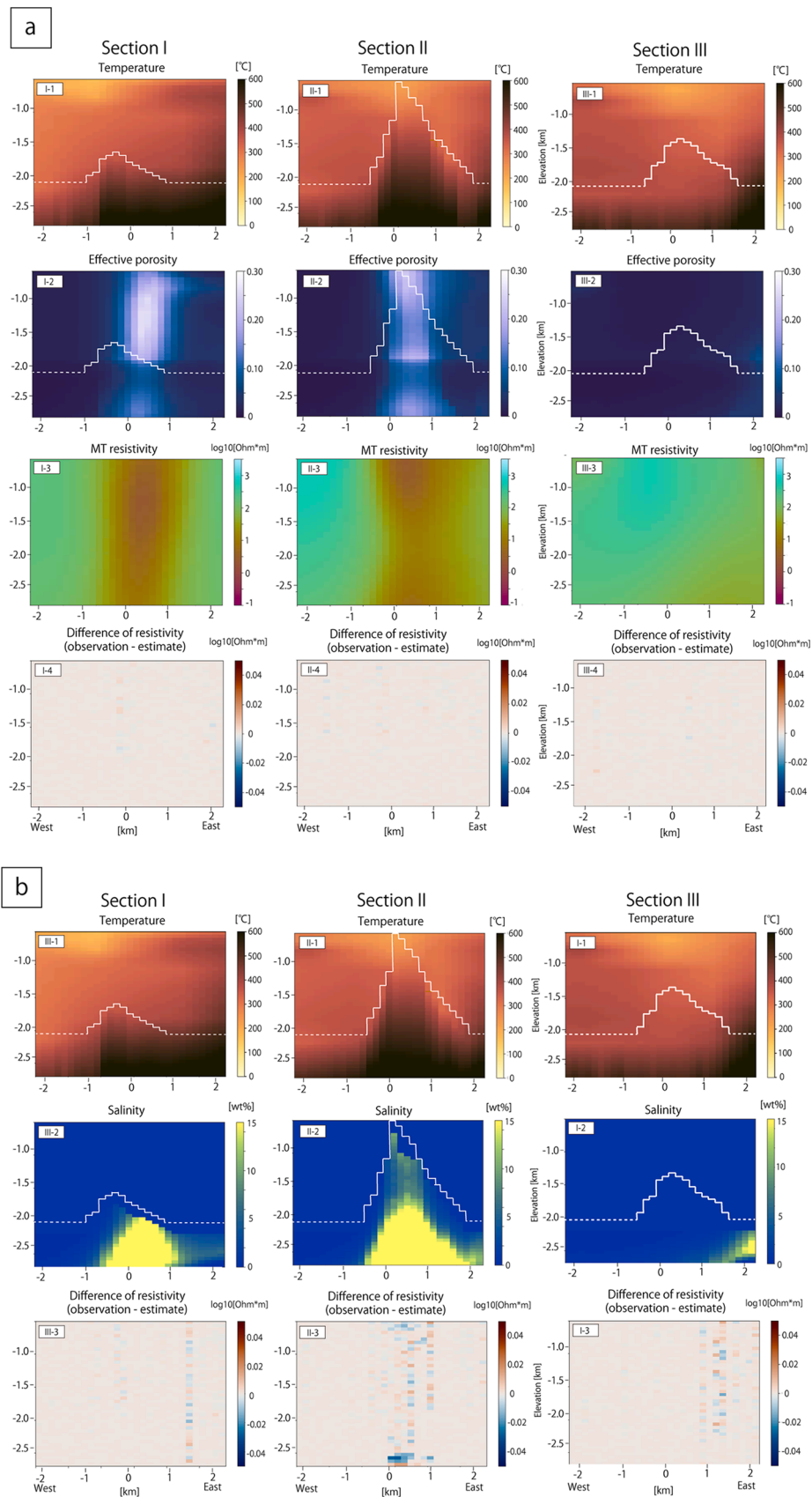
**Fig. 5.** Estimated temperatures and effective porosities/salinities along the WD-1a well in case A (a) and B (b). The black lines indicate reference temperatures along the WD-1a well, and red, blue, and orange lines represent the MAP estimates of temperatures, effective porosities, and salinities, respectively. Red, blue, and orange areas indicate the 95% credible interval of the estimated parameters. Brown horizontal lines indicate the upper boundary of the Kakkonda granite. Error percentages of (a) and (b) were 0.8% and 3.5%, respectively.

Kakkonda granite) were 1.0% (Fig. 7c) and 4.8% (Fig. 7e) in cases A and B, respectively. For further validation, we also calculated the percentage error by performing a comparison with the temperature log along Well-21. The percentage errors along Well-21 were 4.7% in case A (Fig. 7d)

and 3.6% in case B (Fig. 7f) below an elevation of −1900 m. The results show a good agreement as these temperatures were estimated without referring to the deep temperature logs. The estimated temperature patterns mostly follow the shape of the Kakkonda granite (Fig. 7a and

**Fig. 6.** (a) Case A: The series of 1D estimates of estimated temperatures, effective porosities, MT resistivities, and differences between observed and estimated resistivities along sections I (I-1, I-2, I-3, and I-4), II (II-1, II-2, II-3, and II-4), and III in Fig. 5 (III-1, III-2, III-3, and III-4). (b) Case B: The series of 1D estimates of estimated temperatures, salinities, and differences between observed and estimated resistivities along the same sections. White solid and dashed lines in I-1, I-2, II-1, II-2, III-1, and III-2 represent the geological boundaries and the −2.05-km elevation, along which the temperature was estimated using spatial interpolation and the Bayesian framework. We used a scientific colormap by Crameri et al. (2020).
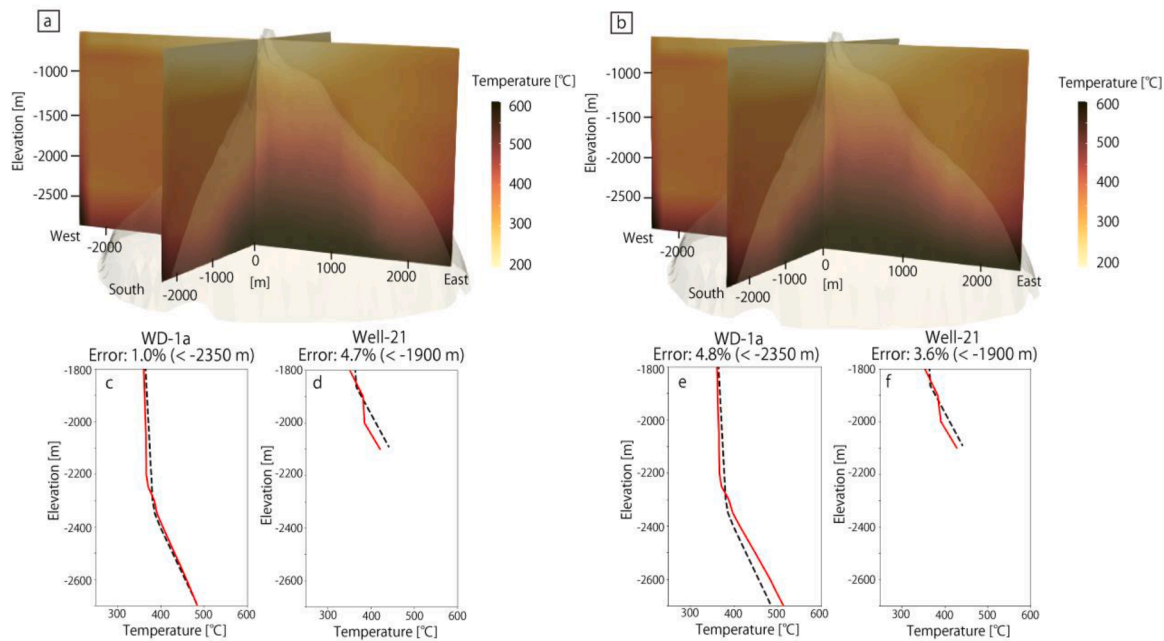
**Fig. 7.** 3D temperature structures in the analysed area in case A (a) and case B (b). The analysed area corresponds to the black rectangle in Fig. 4. The semi-transparent surface overlying the temperature structure represents the upper boundary of the Kakkonda granite. (c)−(f) Comparison of the MAP estimates of the 3D processing (red lines) and reference temperatures (black dashed lines) along WD-1a and Well-21 in case A (c, d) and case B (e, f). For (a) and (b), we used a scientific colormap by Crameri et al. (2020).

7b), which corroborates that the Kakkonda granite is a heat source.

## 5. Discussion

In case A, our result demonstrates that the effective porosity increases with depth at a deep part of the low-resistivity region (Fig. 6a). This estimation does not agree with the general trend in which permeability decreases with depth (Manning and Ingebritsen, 1999). However, in a magmatic-hydrothermal system, the permeability increase may be interpreted because of the pore pressure increase associated with exsolving magmatic fluid. Using a numerical simulation, Weis et al. (2012) and Weis (2015) demonstrated an increase in pore pressure due to the release of magmatic fluids in a ductile region; subsequently, permeability increases approximately 5–10 fold due to the increase in pore pressure. High temperatures (500–600 °C) were registered in areas where the estimated porosity increases with depth, and the lithostatic pressure condition is comparable with the numerical setting used in Weis (2015). Thus, the permeability/porosity increase at depth, proposed by Weis et al. (2012) and Weis (2015), can explain our estimated effective porosity distribution.

In case B, high salinity was inferred around the bottom of the analysed area (Fig. 6b). Studies of fluid inclusions showed that the development of a high salinity (>20wt%) often occurs in the proximity of the fully or partially crystalline magmatic heat sources (e.g. Roedder, 1971, Hedenquist and Lowenstern, 1994; Simmons and Browne, 1997), and it is considered to be the result of condensation and/or boiling of single-phase magmatic fluid. Therefore, our estimated salinity distribution can be interpreted as the result of the phase separation of magmatic saline. As it has been shown that the magnitude of salinity concentration is controlled by several geological factors, including fluid release temperature and magmatic fluid salinity (Afanasyev et al., 2018), the estimated salinity distribution could be used to constrain the magmatic-hydrothermal system by using it to calibrate a numerical simulation. As the NaCl–H₂O resistivity model used in this study has been validated only up to a salinity of 5.6 wt%, we could not obtain a quantitative magnitude of salinity with confidence; however, our results imply high salinity (>15 wt%) may exist in the Kakkonda granite.

Furthermore, because the saline resistivity model has been validated mainly with a single-phase fluid, validation in multiphase (e.g., vapour + liquid coexistence) conditions could be a future research topic.

Notably, although we fixed either effective porosity or salinity in the two cases, both parameters could be variable in a real situation wherein a mix of the cases is observed. For example, in the low resistivity region, effective porosity is high and salinity is moderate/low in a shallow part of the granite (like in case A), whereas salinity is high and effective porosity is moderate/low in a deep part (like in case B). Treating effective porosity, salinity and temperature as variables in our Bayesian framework will be difficult as all the parameters will not be estimated with an acceptable amount of uncertainty. Analysis strategies for such a case where more variables are to be estimated would be a future research topic.

Conductive anomalies at deep locations are sometimes linked with silicate melts (e.g., Heise et al., 2010; Aizawa et al., 2014; Samrocket al., 2021). Around the Kakkonda field, the location of magma is not well known and is difficult to infer because temperature and pressure conditions to generate silicate melts (i.e., the liquidus curve) as well as its mobility highly depend on the water content dissolved in melts (Holtz and Johannes, 1994; Holtz et al., 2001). Nevertheless, we consider unlikely that granitic melts exist in the analysed area because at least a very high pressure (~500 MPa) and high water content (~10 wt%) are required to form melts under the temperature conditions around the bottom of the analysed area (~650 °C) (Holtz et al., 2001).

The existing (shallow) geothermal reservoirs in the Kakkonda field comprise a meteoric-origin fluid with low salinity. One possibility that links the gap between the observed low salinity at shallow locations and the estimated high salinity at deep locations is that magmatic fluid is trapped in the Kakkonda granite. According to previous numerical simulations of the NaCl–H₂O system, the halite precipitation occurred because the phase separation of the NaCl–H₂O system leads to permeability loss and could trap the magmatic fluid (Afanasyev et al., 2018). In addition, silica precipitation due to quartz solubility reduction is expected, especially in the Kakkonda granite (Saishu et al., 2014), and may trap the magmatic fluid.

## 6. Conclusions

Using a Bayesian framework, this study constrains temperatures, effective porosities, and salinities at depth in the Kakkonda geothermal field, Japan, based on MT resistivities. The estimated temperatures follow available deep temperature logs and support the geological interpretation that the Kakkonda granite is a heat source. The two cases we investigated demonstrated that there are still uncertainties, especially with regard to effective porosity and salinity distribution; these uncertainties depend on the geological scenario. Despite this, our results suggest the existence of a magmatic-hydrothermal system at depth in the Kakkonda geothermal field.

The limitation of this approach is its requirement for information regarding a geological boundary of the rock body that serves as the heat source and the conductive temperature pattern within the rock body. However, even where geological boundary data are not available, the proposed Bayesian estimation can be applied to depths if the temperature-at-depth profile shows a thermally conductive pattern.

Bayesian framework estimates parameters with great certainty using an adequate number of observations and certain assumptions. However, data at depth in a geothermal field are often limited. The observations and assumptions used in this study can be applied to a typical geothermal area. Our results suggest that Bayesian rock-physics modelling is effective in estimating temperatures and constraining effective porosity and salinity distribution at depth, even with limited data and assumptions.

## CRediT authorship contribution statement

**Kazuya Ishitsuka:** Conceptualization, Data curation, Formal analysis, Investigation, Methodology, Project administration, Resources, Software, Validation, Visualization, Writing – original draft, Writing – review & editing. **Yusuke Yamaya:** Conceptualization, Investigation, Project administration, Resources, Writing – review & editing. **Norihiro Watanabe:** Conceptualization, Funding acquisition, Investigation, Project administration, Resources, Visualization, Writing – review & editing. **Yosuke Kobayashi:** Investigation, Writing – review & editing. **Toru Mogi:** Conceptualization, Supervision, Writing – review & editing. **Hiroshi Asanuma:** Conceptualization, Funding acquisition, Project administration, Supervision, Writing – review & editing. **Tatsuya Kajiwara:** Data curation, Formal analysis, Resources, Writing – review & editing. **Takeshi Sugimoto:** Data curation, Formal analysis, Resources, Writing – review & editing. **Ryoichi Saito:** Data curation, Formal analysis, Resources, Writing – review & editing.

## Declaration of Competing Interest

The authors declare that they have no known competing financial interests or personal relationships that could have appeared to influence the work reported in this paper.

## Supplementary materials

Supplementary material associated with this article can be found, in the online version, at doi:10.1016/j.geothermics.2021.102316.

## References

Afanasyev, A., Blundy, J., Melnik, O., Sparks, S., 2018. Formation of magmatic brine lenses via focused fluid-flow beneath volcanoes. Earth Planet. Sci. Lett. 486, 119–128. https://doi.org/10.1016/j.epsl.2018.01.013.

Afonso, J.C., Rawlinson, N., Yang, Y., Schutt, D.L., Jones, A.G., Fullea, J., Griffin, W.L., 2016. 3-D multiobservable probabilistic inversion for the compositional and thermal structure of the lithosphere and upper mantle: III. Thermochemical tomography in the western-central U.S. J. Geophys. Res. Solid Earth 121, 7337–7370. https://doi.org/10.1002/2016JB013049.

Aizawa, K., Koyama, T., Hase, H., Uyeshima, M., Kanda, W., Utsugi, M., Yoshimura, R., Yamaya, Y., Hashimoto, T., Yamazaki, K., Komatsu, S., Watanabe, A., Miyawaka, K., Ogawa, Y., 2014. Three-dimensional resistivity structure and magma pluming system of the Kirishima volcanoes as inferred from broadband magnetotelluric data. J. Geophys. Res. Solid Earth 119, 198–215. https://doi.org/10.1002/2013JB01082.

Aizawa, K., Ogawa, Y., Ishido, T., 2009. Groundwater flow and hydrothermal systems within volcanic edifices: delineation by electric self-potential and magnetotellurics. J. Geophys. Res. Solid Earth 114, B01208. https://doi.org/10.1029/2008JB005910.

Akatsuka, T., Saito, R., Kajiwara, T., Osada, K., Nagaso, M., Watanabe, N., Tsuchiya, N., Asanuma, H., Kanetsuki, T., Under review. Geothermal geology and comprehensive temperature model including a deep-seated supercritical geothermal system in Sengan, Northeast Japan, NE Japan, Geothermics, the special issue on "Supercritical Geothermal in Japan".

Archie, G.E., 1942. The electrical resistivity log as an aid in determining some reservoir characteristics. Trans. AIME 146, 54–62. https://doi.org/10.2118/942054-G.

Ardid, A., Dempsey, D., Bertrand, E., Sepulveda, F., Tarits, P., Solon, F., Archer, R., 2021a. Bayesian magnetotelluric inversion using methylene blue structural priors for imaging shallow conductors in geothemal fields. Geophysics 86 (3), E171–E183. https://doi.org/10.1190/GEO2020-0226.1.

Ardid, A., Arher, R., Berrand, E., Sepulveda, F., Tarits, P., Dempsey, D., 2021b. Heat transfer through the Wairakei-Tauhara geothermal system quantified by multi-channel data modeling. Geophys. Res. Lett. 48, e2020GL092056 https://doi.org/10.1029/2020GL092056.

Baker, C.E., Goldstein, R.H., 1990. Fluid-inclusion technique for determining maximum temperature in calcite and its comparison to the vitrinite reflectance geothermometer. Geology 18 (10), 1003–1006. https://doi.org/10.1130/0091-7613(1990)018<1003:FITFDM>2.3.CO;2.

Banerjee, S., Carlin, B.P., Gelfand, A.E., 2015. Hierarchical Modeling and Analysis For Spatial Data, 2nd edition. CRC Press.

Beauchamps, G., Bourdelle, F., Dubois, M., Hebert, R.L., Ledésert, B.A., 2021. First characterization of the cooling of the paleo-geothermal system of Terre-de-Haut (Les Saintes archipelago, Guadeloupe): application of fluid inclusion and chlorite thermometry. J. Volcanol. Geotherm. Res. 419, 107370 https://doi.org/10.1016/j.jvolgeores.2021.107370.

Bredehoeft, J.D., Papaopulos, I.A., 1965. Rates of vertical groundwater movement estimated from the Earth's thermal profile. Water Resour. Res. 1, 325–328. https://doi.org/10.1029/WR001i002p00325.

Browne, P.R.L., 1978. Hydrothermal alteration in active geothermal fields. Ann Rev. Earth Planet. Sci. 6, 229–250. https://doi.org/10.1146/annure.ea.06.050178.001305.

Carpenter, B., Gelman, A., Hoffman, M.D., Lee, D., Goodrich, B., Betancourt, M., Brubaker, M., Guo, J., Li, P., Riddell, A., 2017. Stan: a probabilistic programming language. J. Stat. Softw. 76 (1), 1–32. https://doi.org/10.18637/jss.v076.i01.

Commandeur, J.J.F., Koopman, S.J., 2007. An Introduction to State Space Time Series Analysis. Oxford University Press.

Crameri, F., Shephard, G.E., Heron, P.J., 2020. The misuse of colour in science communication. Nat. Commun. 11, 5444. https://doi.org/10.1038/s41467-020-19160-7.

Dobson, P., Asanuma, H., Huenges, E., Poletto, F., Reinsch, T., Sanjuan, B., 2017. Supercritical geothermal systems – a review of past studies and ongoing research activities. In: Proc. of 41st Workshop on geothermal reservoir engineering SGP-TR-212.

Doi, N., Kato, O., Ikeuchi, K., Komatsu, R., Miyazaki, S., Akaku, K., Uchida, T., 1998. Genesis of the plutonic-hydrothermal system around Quaternary granite in the Kakkonda geothermal system, Japan. Geothermics 27 (5–6), 663–690. https://doi.org/10.1016/S03756505(98)00039-X.

Doi, N., Shigehara, S., Ikeuchi, K., Kato, O., Takahashi, M., Ominato, T., Koide, K., Tosha, T., 2000. Seismic activity in the Kakkonda geothermal system characterized by quaternary Kakkonda granite, Japan. In: Proc. of World Geothermal Congress, 2000, pp. 1077–1082.

Driesner, T., 2007. The system $H_2O$-NaCl. II. Correlations for molar volume, enthalpy, and isobaric heat capacity from 0 to 1000 ℃, 1 to 5000 bar, and 0 to 1 $X_{NaCl}$. Geochim. Cosmochim. Acta 71, 4902–4919.

Driesner, T., Heinrich, C.A., 2007. The system $H_2O$-NaCl. I. Correlation formulae for phase relations in temperature-pressure-composition space from 0 to 1000 ℃, 0 to 5000 bar, and 0 to 1 $X_{NaCl}$. Geochim. Cosmochim. Acta 71, 4880–4901. https://doi.org/10.1016/j.gca.2006.01.033.

Elders, W.A., Friðleifsson, G.Ó., Pálsson, B., 2014. Iceland Deep Drilling Project: the first well, IDDP-1, drilled into magma. Geothermics 49 (1). https://doi.org/10.1016/j.geothermics.2013.08.012.

Friðleifsson, G.Ó., Elders, W.A., Zierenberg, R.A., Stefánsson, A., Fowler, A.P.G., Weisenberger, T.B., Haðarson, B.S., Mesfin, K.G., 2017. The Iceland Deep Drilling Project 4.5 km deep well, IDDP-2, in the seawater-recharged Reykjanes geothermal field in SW Iceland has successfully reached its supercritical target. Sci. Drill. 23 https://doi.org/10.5194/sd-23-1-2017.

Fujimoto, K., Takahashi, M., Doi, N., Kato, O., 2000. High permeability of Quaternary granites in the Kakkonda geothermal area, northeast Japan. Proceed. World Geother. Congr. 2000, 1139–1144.

Gelman, A., 2006. Prior distributions for variance parameters in hierarchical models (comment on article by Browne and Draper). Bayesian Anal. 1 (3), 515–534. https://doi.org/10.1214/06-BA117A.

Gelman, A., Rubin, D.B., 1992. Inference from iterative simulation using multiple sequences. Stat. Sci. 7 (4), 457–472. https://doi.org/10.1214/ss/1177011136.

Gelman, A., Carlin, J.B., Stern, H.S., Dunson, D.B., Vehtari, A., Rubin, D.B., 2013. Bayesian Data Analysis, 3rd ed. CRC Press, pp. 261–310.

Geman, S., Geman, D., 1984. Stochastic relaxation, Gibbs distributions and the Bayesian restoration of images. IEEE Trans. Pattern Anal. Mach. Intell. 6, 721–741. https://doi.org/10.1109/TPAMI.1984.476596.

Glover, P.W.J., Hole, M.J., Pous, J., 2000. A modified Archie's law for two conducting phases. Earth Planet. Sci. Lett. 180 (3–4), 369–383. https://doi.org/10.1016/S0012-821X(00)00168-0.

Gunnarsson, G., Arnaldsson, A., Oddsdóttir, A.L., 2011. Model simulations of the Hengill area, Southwestern Iceland. Transp. Porous Media 90 (1), 3–22. https://doi.org/10.1007/s11242-010-9629-1.

Heinrich, C.A., 2005. The physical and chemical evolution of low-salinity magmatic fluids at the porphyry to epithermal transition: a thermodynamic study. Miner. Deposita 39, 864–889. https://doi.org/10.1007/s00126-004-0461-9.

Heinrich, C.A., 2007. Fluid-fluid interactions in magmatic-hydrothermal ore formation. Revi. Mineral. Geochem. 65 (1), 363–387. https://doi.org/10.2138/rmg.2007.65.11.

Heise, W., Caldwell, T.G., Bibby, H.M., Bannister, S.C., 2008. Three-dimensional modeling of magnetotelluric data from the Rotokawa geothermal field Taupo volcanic zone, New Zealand. Geophys. J. Int. 173 (2), 740–750. https://doi.org/10.1111/j.1365-246X.2008.03737.x.

Heise, W., Caldwell, T.G., Bibby, H.M., Bennie, S.L., 2010. Three-dimensional electrical resistivity image of magma beneath an active continental rift, Taupo Volcanic Zone, New Zealand. Geophys. Res. Lett. 37, L10301. https://doi.org/10.1029/2010GL043110.

Hedenquist, J.W., Lowenstern, J.B., 1994. The role of magmas in the formation of hydrothermal ore-deposits. Nature 370, 519–527. https://doi.org/10.1038/37051a0.

Hoffman, M.D., Gelman, A., 2014. The No-U-Turn sampler: adaptively setting path lengths in Hamiltonian Monte Carlo. J. Mach. Learn. Res. 15, 1593–1623.

Hokstad, K., Tänavsuu-Milkeviciene, K., 2017. Temperature prediction by multigeophysical inversion: application to the IDDP-2 well at Reykjanes, Iceland. GRC Trans. 41.

Holtz, F., Johannes, W., 1994. Maximum and minimum water contents of granitic melts: implications for chemical and physical properties of ascending magmas. Lithos 32, 149–159. https://doi.org/10.1016/0024-4937(94)90027-2.

Holtz, F., Johannes, W., Tamic, N., Behrens, H., 2001. Maximum and minimum water contents of granitic melts generated in the crust: a reevaluation and implications. Lithos 56, 1–14. https://doi.org/10.1016/S0024-4937(00)00056-6.

Ikeuchi, K., Doi, N., Sakagawa, Y., Kamenosono, H., Uchida, T., 1998. High-temperature measurement in well WD-1a and the thermal structure of the Kakkonda geothermal system, Japan. Geothermics 27 (5/6), 591–607. https://doi.org/10.1016/S0375-6505(98)00035-2.

Ishitsuka, K., Mogi, T., Sugano, K., Yamaya, Y., Uchida, T., Kajiwara, T., 2018. Resistivity-based temperature estimation of the Kakkonda geothermal field, Japan, using a neural network and neural kriging. IEEE Geosci. Remote Sens. Lett. 15 (8), 1154–1158. https://doi.org/10.1109/LGRS.2018.2832647.

Ishitsuka, K., Kobayashi, Y., Watanabe, N., Yamaya, Y., Bjarkason, E., Suzuki, A., Mogi, T., Asanuma, H., Kajiwara, T., Sugimoto, T., Saito, R., 2021. Bayesian and neural network approaches to estimate deep temperature distribution for assessing a supercritical geothermal system: evaluation using a numerical model. Nat. Resour. Res. https://doi.org/10.1007/s11053-021-09874-w.

Jalilinarabady, S., Itoi, R., Gotoh, H., Tanaka, T., 2011. Development of the optimum numerical reservoir model of the Takigami geothermal field, Oita, Japan. In: Proc. 36th Workshop on Geothermal Reservoir Engineering.

Kasai, K., Sakagawa, Y., Komatsu, R., Sasaki, M., Akaku, K., Uchida, T., 1998. The origin of hypersaline liquid in the Quaternary Kakkonda granite, sampled from well WD-1a, Kakkonda geothermal system, Japan. Geothermics 27 (5/6), 631–645. https://doi.org/10.1016/S0375-6505(98)00037-6.

Kato, O., Doi, N., Muramatsu, Y., 1993. Neo-granitic pluton and geothermal resercoir at the Kakkonda geothermal field, Iwate prefecture, Japan. J. Geotherm. Res. Soc. Jpn. 15 (1), 41–57 (in Japanese with English abstract).

Kato, O., Doi, N., Ikeuchi, K., Kondo, T., Kamenosono, H., Yagi, M., Uchida, T., 1996. Characteristics of temperature curves and fracture systems in Quaternary Granite and Tertiary pyroclastic rocks of NEDO WD-1a in the Kakkonda geothermal field. In: Japan, 8th International Symposium on the Observation of the Continental Crust Through Drilling, pp. 241–246.

Kitagawa, G., 1987. Non-Gaussian state–space modeling of nonstationary time series. J Am Stat Assoc 82 (400), 1032–1041. https://doi.org/10.1080/01621459.1987.10478534.

Kitagawa, G., 1996. Monte Carlo filter and smoother for non-Gaussian nonlinear state-space models. J. Comput. Graph. Statist. 5, 1–25. https://doi.org/10.1080/10618600.1996.10474692.

Kitagawa, G., Matsumoto, N., 1996. Detection of coseismic changes of underground water level. J Am Stat Assoc 91, 521–528. https://doi.org/10.1080/01621459.1996.10476917.

Kummerow, J., Raab, S., 2015. Temperature dependence of electrical resistivity – Part I: experimental investigations of hydrothermal fluids. Energy Procedia 76, 240–246. https://doi.org/10.1016/j.egypro.2015.07.854.

Liebscher, A., Heinrich, C.A., 2007. Fluid-fluid interactions in the Earth's lithosphere. Rev. Mineral. Geochemi. 65, 1–13. https://doi.org/10.2138/rmg.2007.65.1.

Manning, C.E., Ingebrtsen, S.E., 1999. Permeability of the continental crust: implications of geothermal data and metamorphic systems. Rev. Geophys. 37, 127–150. https://doi.org/10.1029/1998RG900002.

Metropolis, N., Rosenbluth, A., Rosenbluth, M., Telluer, M., Teller, E., 1953. Equations of state calculations by fast computing machines. J. Chem. Phys. 21, 1087–1092. https://doi.org/10.1063/1.1699114.

Mogi, T., Nakama, S., 1993. Magnetotelluric interpretation of the geothermal system of the Kuju volcano, southwest Japan. J. Volcanol. Geotherm. Res. 56, 297–308. https://doi.org/10.1016/0377-0273(93)90022-J.

Neal, R., 2011. Handbook of Marcov Chain Monte Carlo, Chapter 5: MCMC Using Hamiltonian dynamics. CRC press.

New Energy and Industrial Technology Development Organization (NEDO), 1990. Report of Nationwide Geothermal Resources Exploration Project (3rd Phase) in FY 1990, Regional Exploration of Geothermal Fluid Circulation System, Akitakoma area, Resistivity (MT and AMT Method), p. 253 p(in Japanese).

New Energy and Industrial Technology Development Organization (NEDO), 1999. Report On Verification of Geothermal Exploration Technologies in FY 1998, Deep-seated geothermal Resources Survey, p. 1118 (in Japanese).

New Energy and Industrial Technology Development Organization (NEDO), 2019. Review of Potential Supercritical Geothermal Resources to 5 Km in Japan. Technical Report 20190000000100. (in Japanese).

Nono, F., Gibert, B., Parat, F., Loggia, D., Cichy, S.B., Violay, M., 2020. Electrical conductivity of Icelandic deep geothermal reservoirs up to supercritical conditions: insight from laboratory experiments. J. Volcanol. Geotherm. Res. 392 (1), 106364 https://doi.org/10.1016/j.jvolgeores.2018.04.021.

Okamoto, K., Asanuma, H., Ishibashi, T., Yamaya, Y., Saishu, H., Yanagisawa, N., Mogi, T., Tsuchiya, N., Okamoto, A., Naganawa, S., Ogawa, Y., Ishitsuka, K., Fujimitsu, Y., Kitamura, K., Kajiwara, T., Horimoto, S., Shimada, K., 2019. Geological and engineering features of developing ultra-high-temperature geothermal systems in the world. Geothermics 82, 267–281. https://doi.org/10.1016/j.geothermics.2019.07.002.

Olhoeft, G.R., 1981. Electrical properties of granite with implications for the lower crust. J. Geophys. Res. 86 (B2), 931–936. https://doi.org/10.1029/JB086iB02p00931.

O'Sullivan, M.J., Pruess, K., Lippmann, M.J., 2001. State of the art of geothermal reservoir simulation. Geothermics 30 (4), 395–429. https://doi.org/10.1016/S0375-6505(01)00005-0.

Qashqai, M.T., Afonso, J.C., Yang, Y., 2018. Physical state and structure of the crust beneath the western-central United States from multiobservable probabilistic inversion. Tectonics 37 (9), 3117–3147. https://doi.org/10.1029/2017TC004914.

Reinsch, T., Dobson, P., Asanuma, H., Huenges, E., Poletto, F., Sanjuan, B., 2017. Utilizing supercritical geothermal systems: a review of past ventures and ongoing research activities. Geotherm. Energy 5, 16. https://doi.org/10.1186/s40517-017-0075-y.

Roedder, E., 1971. Fluid inclusion studies on the porphyry-type ore deposits at Bingham, Utah, Butte, Montana, and Climax, Colorado. Econ. Geol. 66, 98–118. https://doi.org/10.2113/gsecongeo.66.1.98.

Saishu, H., Okamoto, A., Tsuchiya, N., 2014. The significance of silica precipitation on the formation of the permeable-impermeable boundary within Earth's crust. Terra Nova 26 (4), 253–259. https://doi.org/10.1111/ter.12093.

Samrock, F., Grayver, A.V., Bachmann, O., Karakas, Ö., Saar, M.O., 2021. Integrated magnetotelluric and petrological analysis of felsic magma reservoirs: insights from Ethiopian rift volcanoes. Earth Planet. Sci. Lett. 559, 116765 https://doi.org/10.1016/j.epsl.2021.116765.

Scott, S., Driesner, T., Weis, P., 2015. Geologic controls on supercritical geothermal sources above magmatic intrusions. Nat. Commun. 6, 7837. https://doi.org/10.1038/ncomms8837.

Scott, S., Driesner, T., Weis, P., 2017. Boiling and condensation of saline geothermal fluids above magmatic intrusions. Geophys. Res. Lett. 44 (4), 1696–1705. https://doi.org/10.1002/2016GL071891.

Sepúlveda, F., Rosenberg, M.D., Rowland, J.V., Simmons, S.F., 2012. Kriging predictions of drill-hole stratigraphy and temperature data from the Wairakei geothermal field, New Zealand: implications for conceptual modeling. Geothermics 42, 13–31. https://doi.org/10.1016/j.geothermics.2012.01.002.

Siripunvaraporn, W., Egbert, G., 2009. WSINV3DMT: vertical magnetic field transfer function inversion and parallel implementation. Phys. Earth Planet. Inter. 173 (3–4), 317–329. https://doi.org/10.1016/j.pepi.2009.01.013.

Simmons, S.F., Browne, P.R.L., 1997. Saline fluid inclusions in sphalerite from the Broadlands-Ohaaki geothermal system: a coincidental trapping of fluids being boiled toward dryness. Econ. Geol. 92, 485–489. https://doi.org/10.2113/gsecongeo.92.4.485.

Sinmyo, R., Keppler, H., 2017. Electrical conductivity of NaCl-bearing aqueous fluids to 600℃ and 1 GPa. Contrib. Mineral. Petrol.s 172 (4). https://doi.org/10.1007/s00410-016-1323-z.

Spichak, V., Geiermann, J., Zakharova, O., Calcagno, P., Genter, A., Schill, E., 2015. Estimating deep temperatures in the Soultz-sous-Forets geothermal area (France)

from magnetotelluric data. Near Surface Geophys. 13 (4), 397–408. https://doi.org/10.3997/1873-0604.2015014.

Spichak, V.V., Zakharova, O.K., Goidina, A.G., 2013. A new conceptual model of the Icelandic crust in the Hengill geothermal area based on the indirect electromagnetic geothermometry. J. Volcanol. Geotherm. Res. 257 (1), 99–112. https://doi.org/10.1016/j.jvolgeores.2013.03.013.

Tanaka, A., Ishikawa, Y., 2002. Temperature distribution and focal depth in the crust of the northeastern Japan. Earth Planet. Space 54, 1109–1113. https://doi.org/10.1186/BF03353310.

Tseng, K.H., Ogawa, Y., Nurhasan, Tank, S.B., Ujihara, N., Honkura, Y., Terada, A., Usui, Y., Kanda, W., 2020. Anatomy of active volcanic edifice at the Kusatsu-Shirane volcano, Japan, by magnetotellurics: hydrothermal implications for volcanic unrests. Earth Planet. Space 72 (161). https://doi.org/10.1186/s4623-020-01283-2.

Tole, M.P., Armannsson, H., Zhong-He, P., Arnósson, S., 1993. Fluid/mineral equilibrium calculations for geothermal fluids and chemical geothermometry. Geothermics 22 (1), 17–37. https://doi.org/10.1016/0375-6505(93)90018-1.

Tosha, T., Sugihara, M., Nishi, Y., 1998. Revised hypocenter solutions for microearthquakes in the Kakkondageothermal field, Japan. Geothermics 27 (5/6), 553–571.

Uchida, T., Ogawa, Y., Takakura, S., Mitsuhata, Y., 2000. Geoelectrical investigation of the Kakkonda geothermal field, northern Japan. Proceed. World Geotherm. Congr. 2000, 1893–1898.

Weis, P., Driesner, T., Heinrich, C.A., 2012. Porphyry-copper ore shells form at stable pressure-temperature fronts within dynamic fluid plumes. Science 338 (6114), 1613–1616. https://doi.org/10.1126/science.1225009.

Weis, P., 2015. The dynamic interplay between saline fluid flow and rock permeability in magmatic-hydrothermal systems. Geolfuids 15, 350–371. https://doi.org/10.1111/gfl.12100.

Yamaya, Y., Suzuki, Y., Murata, Y., Okamoto, K., Watanabe, N., Asanuma, H., Hase, H., Ogawa, Y., Mogi, T., Ishizu, K., Uchida, T., 3-D resistivity imaging of the supercritical geothermal system in Sengan geothermal region, NE Japan, Earth and Space Science Open Archive. https://doi.org/10.1002/essoar.10509292.1.

Zuza, A.V., Cao, W., 2020. Seismogenic thickness of California: implication for thermal structure and seismic hazard. Tectonophysics 782-783, 228426. https://doi.org/10.1016/j.tecto.2020.228426.